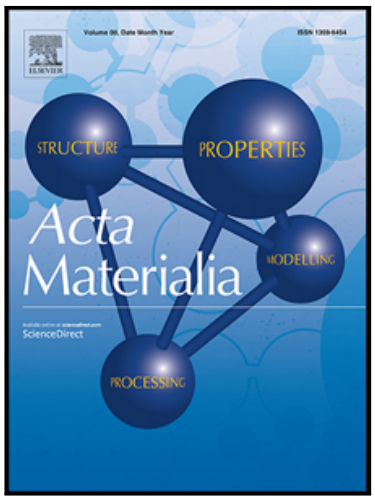

Towards understanding grain nucleation under Additive Manufacturing solidification conditions

Arvind Prasad , Lang Yuan , Peter Lee , Mitesh Patel , Dong Qiu , Mark Easton , David StJohn

PII: S1359-6454(20)30351-7
DOI: https://doi.org/10.1016/j.actamat.2020.05.012
Reference: AM 16022

To appear in: *Acta Materialia*

Received date: 16 January 2020
Revised date: 1 May 2020
Accepted date: 4 May 2020

Please cite this article as: Arvind Prasad , Lang Yuan , Peter Lee , Mitesh Patel , Dong Qiu , Mark Easton , David StJohn , Towards understanding grain nucleation under Additive Manufacturing solidification conditions, *Acta Materialia* (2020), doi: https://doi.org/10.1016/j.actamat.2020.05.012

Towards understanding grain nucleation under Additive Manufacturing solidification conditions

Arvind Prasad[a], Lang Yuan[b], Peter Lee[c], Mitesh Patel[d], Dong Qiu[d], Mark Easton[d], David StJohn[a]

[a]School of Mechanical and Mining Engineering, University of Queensland, Brisbane, 4072, QLD, Australia

[b]Mechanical Engineering, College of Engineering and Computing, University of South Carolina, USA

[c]Mechanical Engineering, University College London, London, WC1E 7JE, UK

[d] RMIT Centre for Additive Manufacturing, School of Engineering (Materials and Manufacturing), RMIT University, 115 Queensberry Street, Carlton 3053, VIC, Australia

Graphical abstract

Transition from solutal to thermal undercooling promotes additional nucleation events

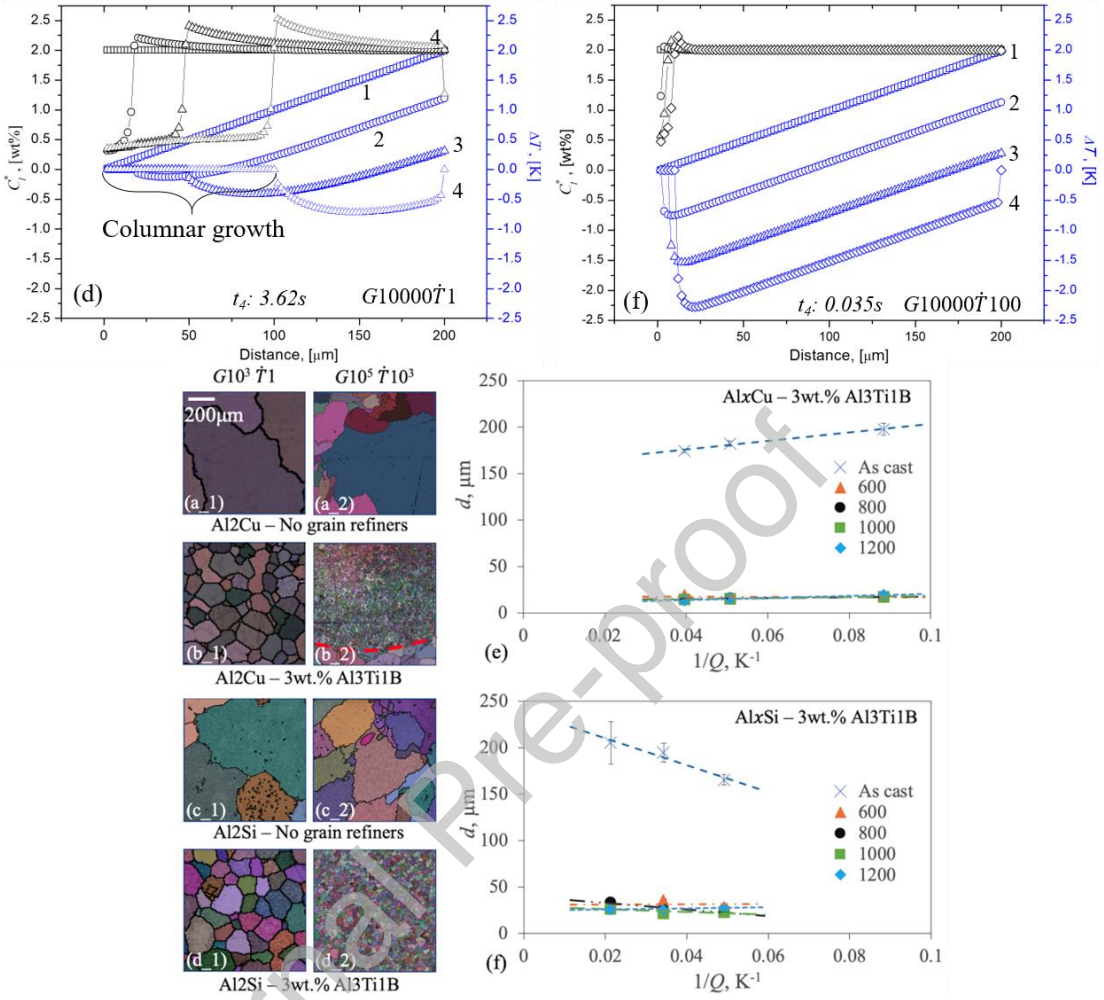

Abstract:

This paper provides insights into the effect of high thermal gradients and cooling rates on equiaxed grain nucleation and growth in conditions similar to those experienced during Additive Manufacturing (AM) processes. Bridgman type solidification is numerically simulated with columnar grains growing at a fixed pull rate under a user-imposed thermal gradient. Controlled inoculants of known nucleation undercooling were placed ahead of the growing columnar grains to allow quantitative analysis of nucleation events. At low thermal gradient and cooling rate only the inoculants with low nucleation undercooling were activated due to low melt undercooling driven by constitutional supercooling (*CS)*. As the cooling rate is increased, for a given thermal gradient, a larger number of inoculants with higher nucleation undercoolings were activated. At higher cooling rates, thermal undercooling was generated by a lag in the growth rate of the solid-liquid (S-L) interface compared to the theoretical pull rate. Thus, thermal undercooling becomes dominant leading to the facilitation of nucleation on less potent substrates requiring higher undercooling. The results show a transition from solute-driven undercooling to cooling rate driven thermal undercooling which contributes to the undercooling that activates the nucleation events. Invoking the Interdependence model, it is also shown that the high cooling rate induced thermal undercooling reduces the size of the nucleation free zone substantially.

Keywords: Additive Manufacturing, Columnar-to-Equiaxed Transition (CET), Cooling rate, Interdependence Model, Numerical Simulation

1. Introduction

Additive Manufacturing is a rapidly growing materials processing route. It is now established that the potential functional advantages with greater design freedom enabled by layer-by-layer manufacturing can be coupled with improved properties [1, 2]. These accrued advantageous properties are often believed to be due to the extreme solidification conditions prevalent in AM processes resulting in unique microstructures. In particular, AM processes are exposed to high temperature gradients and high cooling rates, several orders of magnitude higher than in conventional castings [3]. A review of the literature suggests that depending upon the process, the thermal gradient can range from 10^5 to 10^7 Km^{-1} and the cooling rates can vary between 10^2 and 10^6 Ks^{-1} [4-19]. For instance, Kar and Mazumder [4] cite 10^2 Ks^{-1} for their laser cladding process, while Hofmeister et al [8] report that the cooling rate can vary between 200-6000 Ks^{-1} during the LENS process.

There are several examples available in the literature where unique microstructures are reported from AM processes [20-23]. Although these reports offer a good insight into possible microstructural variations during AM, in the summary of their recent review article on mechanical properties obtained in AM processes, Lewandowski and Seifi [1] conclude that strategies are required to take advantage of the microstructures possible with AM processes. One such possible strategy is to engineer the microstructure during AM processing which in turn requires insights into the mechanisms of microstructure formation. While there are a number of ways to engineer the structure during processing and thus influence the performance (e.g. see Figure 1 in [24]), the current work focuses on understanding grain nucleation and growth of grains under extreme cooling conditions as experienced during AM.

1.1 Columnar to Equiaxed Transition (CET) during AM related processes

The CET during conventional solidification has been of interest for a long time. Significant research has been conducted in this area both mathematically, e.g. [25-30], as well as experimentally [3, 31]. The studies have shown that undercooling ahead of the columnar grains is critical for equiaxed grains to nucleate and grow [28, 29]. For Columnar-to-Equiaxed (CET) studies using *μMatIC*, Dong and Lee [29] concluded that the solute profile ahead of the advancing interface is critical for CET and that 'still more information is required about the density and activation of nuclei if accurate predictions are to be made.'

The undercooling provided by the solute in the liquid ahead of the growing S-L interface is called Constitutional Supercooling, *CS*. This is useful both for the further growth of the interface as well as activating a new nucleation event ahead of the growing interface [32]. The Interdependence Model quantifies different components that facilitate the development of *CS* which subsequently are used to predict a new nucleation event and the resulting grain size [32, 33].

One of the significant challenges in AM is the propensity for columnar grain structures to often have undesired anisotropic properties. A few numerical studies have been published regarding the CET in AM processes. These studies confirm some of the observations from the previous research regarding CET, namely, the role of a critical nucleation undercooling ΔT_n [34], constitutional supercooling ΔT_{CS}, [35], thermal gradient [36-39], and the inoculant density [34, 40].

Experimental verification of CET in AM processes include the results from Bermingham et al [41] who reported a mix of columnar and equiaxed grains in Ti-alloys with La_2O_3 particles produced by a wire based AM process. Hadadzadeh et al [42] reported CET in an AlMgSi alloy under Direct Metal Laser Sintering (DMLS) being dependent on the build direction.

Wang et al [43] obtained a mix of columnar and equiaxed grains during the WAAM process for Ti6Al4V alloy. Bai et al [44, 45] investigated laser melted and deposited experiments on a V-5Cr-5Ti alloy, where they reported initially forming coarse columnar grains changing to fine columnar grains and then, finally, to a small region of equiaxed grains.

Research that defines processing windows to achieve a desired microstructure has also been important. For instance, Dantzig & Rappaz developed a thermal gradient, *G*, and pull rate, *V* (*G-V)* plot with a CET zone and various processes marked on the plot [46]. From a fundamental solidification point of view, the formation of equiaxed grains ahead of the columnar grains in the AM process is essentially a CET event. Factors leading to the establishment of a critical amount of undercooling required for activating equiaxed grain nucleation are not addressed in these plots and therefore do not highlight the mechanisms that lead to the promotion or inhibition of CET. In particular, the role of the thermal gradient, *G*, and cooling rate, $\dot{T}$, in establishing a minimum undercooling ΔT_n required to activate equiaxed grains is not clear. Moreover, the extent of *CS* in the presence of a high thermal gradient is not clear.

The present work studies the CET for a range of thermal gradients and cooling rates to understand the role of these factors in solute distribution and eventual undercooling and uses the Interdependence Model [32] to highlight the role of a developing solute profile ahead of an advancing interface in establishing the required undercooling. Finally, the current approach is not to model a particular AM process per se but to gain insights into the nucleation phenomena and solidification conditions leading to CET in AM processes.

2. Approach

AM processes undergo complex thermal processing cycles, which necessitates better understanding of microstructure, process and properties for the AM processes [47]. The

purpose of this work is to investigate the conditions that facilitate nucleation which can lead to smaller equiaxed grain sizes during an AM process under different combinations of G and $\dot{T}$.

Although previous studies have established that a range of microstructures are possible under a range of cooling rates, the numerical model, *μMatIC*, is used to study grain nucleation under the thermal conditions (G and $\dot{T}$) expected in typical AM processes. Towards this goal, equiaxed grain formation ahead of a set of growing columnar grains under a range of thermal gradients and cooling rates was studied. One of the salient features of the Interdependence Model is that it quantifies the role of solute diffusion (via solute diffusion length) in predicting the onset of a nucleation event. Here, the interplay between ΔT_{CS} generated from a growing grain and the imposed G and $\dot{T}$ and their respective role in activating a nucleation event is explored. The advantage of this approach is that an undercooling nucleation law, such as ΔT_n following a particular distribution, is not imposed in the simulations. Therefore, the solute contribution from the growing columnar grains in establishing the required undercooling can be studied. Note that the Interdependence Model was developed for equiaxed growth only and therefore the present work is an extension of the Interdependence Model to study the applicability of this model for studying the columnar to equiaxed transition as well. In effect then, this work considers the solute content at the interface of the already nucleated and growing grain regardless of their morphology.

Furthermore, although a typical AM process may involve repeated heating and cooling cycles, only the simulation of the solidification of a melt pool during a single cycle is considered. Pre-fixed nucleated grains are allowed to grow into the melt pool where a fixed G is imposed from top (higher temperature) to bottom (lower temperature). A fixed cooling rate, $\dot{T}$, is imposed which acts throughout the solidification process, which in turn fixes the

pull rate V for Bridgman solidification. Fixed G and V conditions facilitate the explanation based on the Interdependence Model.

μMatIC is a microscale solidification code based on the Cellular Automaton (CA) approach. In the past it has been successfully used to model CET for casting conditions, and porosity and microstructure formation [48-53], as well as validating the Interdependence Model [54]. The details of the *μMatIC* model have been presented elsewhere [50, 52].

In the model, the solutal and thermal conservation equations are solved, which determines the time-dependent solid fraction. Therefore, the tip growth rate is determined dynamically from the solutal undercooling. The model assumes local equilibrium at the S-L interface. The attachment kinetics leading to non-equilibrium effects such as a velocity dependent partition coefficient, k_v are not incorporated in the current study.

Lee and co-authors previously published their work on CET using *μMatIC* for more conventional solidification conditions [29, 55]. There a solute adjusted undercooling was used as the nucleation threshold for the entire melt (computational domain), wherein the inoculant undercoolings were assumed to have a Gaussian distribution. The computation consisted of ascertaining the amount of undercooling ahead of advancing columnar dendritic grains in the presence of a thermal gradient and local solute concentration. As the bulk threshold of undercooling was reached at a specific location, any inoculant present would activate a nucleation event. For the present study, a different approach is taken where individual inoculants have been assigned a specific value of ΔT_n (with respect to the alloy liquidus, T_l) at or below which it triggers a nucleation event. This is a different approach since the model can take into account a number of important parameters, viz., the particle size distribution, the number density of the inoculants as well as individual particle ΔT_n values as required.

In actual practice, the inoculants placed within the melt comprise a range of sizes with a range of corresponding undercooling (ΔT_n) at which they would activate a nucleation event [56]. To make the model simulate this behaviour, the model was modified to enable assigning a specific value of ΔT_n for each inoculant particle placed within the computational domain. An inoculant particle is 'placed' at any given location within the domain by assigning the coordinates of that location [X, Y, Z] and the ΔT_n assigned to the inoculant present at that particular location [X, Y, Z, ΔT_n]. Computationally, it means that when the inoculant location temperature reaches ($T_l - \Delta T_n$) or lower, a nucleation event will be activated at that location. This modification allows testing more realistic scenarios and allows validation of models that follow the solute paradigm of nucleation [57].

With the z-axis set to only 1 cell thick, the computation can be approximated as 2-D. G and $\dot{T}$ are kept constant and gravity and fluid convection effects have been neglected in the present study. Previous work using *μMatIC* [52] has shown that transportation of solute species via convection currents affects the growth rate both during constrained and free growth and that 3-D models are more suitable to capture these effects. Moreover, with Cu being much denser than Al in the Al-Cu system modelled in the current work, the gravity effects are also expected to move the nucleated equiaxed grains, altering the Cu concentration around the growing dendrite tips thus affecting their growth rates [58]. For the current study, analysis of such complex interplay has not been considered and the focus is only on the interplay between cooling rates and thermal gradients. Furthermore, because the aim is to study the nucleation events of inoculants and therefore grain orientation and crystallography during solidification are not considered stochastically.

Table 1. Thermo-physical properties of the alloy and phase diagram information for the Al-2Cu alloy used in the simulations [59].

	Al-2wt%Cu	
	Value	[Units]
T_l, alloy liquidus	929	[K]
T_s, alloy solidus	821	[K]
m, liquidus slope	-2.6	[K/%]
k_e, partition coefficient	0.14	[-]
D_l, Solute liquid diffusion	$3x10^{-9}$	$[m^2s^{-1}]$
D_s, Solute solid diffusion	$3x10^{-12}$	$[m^2s^{-1}]$
L, heat of fusion	$9.63x10^{+8}$	$[Jm^{-3}]$
C_p, alloy specific heat	1042	$[Jkg^{-1}K^{-1}]$
ρ, alloy density	$2.5x10^{+3}$	$[kgm^{-3}]$
k, thermal conductivity	25	$[Wm^{-1}K^{-1}]$
γ, Surface tension	0.095	Nm^{-1}
Γ, Gibbs-Thomson coeff.	$0.9x10^{-7}$	[K m]

The simulations were performed for an Al-2wt%Cu alloy. The Al-Cu system has been well studied in the past and therefore the current work lends itself easily to comparison. Table 1 shows the thermophysical properties and the phase diagram parameters for the Al-2wt%Cu alloy.

Following the satisfactory results from the 'inoculant-undercooling' test presented in Appendix A, further simulations were carried out to study equiaxed grain formation under a

range of cooling conditions with the cell size of 2 μm, which is sufficient to reveal both first and secondary dendrite arms. The simulation conditions carried out are listed in Table 2 and are typical of the cooling conditions (G and $\dot{T}$) reported in the literature [4, 8, 16, 17, 19]. The wide range of thermal gradients used in the test conditions are classified into "low", "medium" and "high" G. The "low" G condition is comprised of runs with G = 500 Km^{-1} and cooling rates of 0.25 Ks^{-1} and 100 Ks^{-1} (identified as $G500\dot{T}0.25$ and $G500\dot{T}100$ respectively). The "medium" and "high" G simulations have gradients of 1000 Km^{-1} and 10000 Km^{-1} respectively and include a range of cooling rates from 1 Ks^{-1} to 100 Ks^{-1}.

3. Results

Figure 1 shows the computational domain, 1000 μm x 1000 μm, for simulation cases presented in Table 2. Twenty grains starting from the bottom wall are allowed to grow simulating a Bridgman solidification condition with fixed G and $\dot{T}$ (Table 2). The imposed $\dot{T}$ is obtained by setting a fixed pull rate. The bottom grains either simulate the multiple nucleation events on the surface of the mould wall due to thermal undercooling (ΔT_{therm}), or epitaxial growth observed in AM processes. These grains nucleate at the alloy liquidus and grow directionally as columnar grains. Five inoculants are placed at 200 μm from the bottom wall, each assigned a different value of ΔT_n. The inoculants are also placed at a spacing of 200 μm. The increase in ΔT_n from left to right – from 0.1 K to 2.0 K – is marked in Figure 1. A thermal gradient is imposed from top to bottom, the top wall being at a higher temperature. The orientation of the computational domain is indicated in the figure inset

Table 2. Simulation cases for CET studies during different solidification conditions for the Al-2wt%Cu alloy.

G [Km^{-1}]	$\dot{T}$ [Ks^{-1}]	Identification	($\dot{T}/G$) ratio [m/s]	Classification
500	0.25	$G500\dot{T}0.25$	0.0005	Low G
	100	$G500\dot{T}100$	0.2	
1000	1	$G1000\dot{T}1$	0.001	Medium G
	10	$G1000\dot{T}10$	0.01	
	100	$G1000\dot{T}100$	0.1	
10000	1	$G10000\dot{T}1$	0.0001	High G
	10	$G10000\dot{T}10$	0.001	
	100	$G10000\dot{T}100$	0.01	

3.1 Low temperature gradient

Figure 2 shows the result for the 'low' G condition. The initial twenty columnar grains grow with a cellular morphology. As shown in Figure 2a, only three nucleation events occurred (0.1, 0.2, 0.5 K) for the low $\dot{T}$ condition. The relatively large size of the growing equiaxed grains suggests that the grains were nucleated early, allowing them to grow back towards the growing columnar grains. These observations are further explained in the 'Discussion' section (Section 4) with reference to Figure 3. The middle grain with ΔT_n of 0.5 K was nucleated later and is therefore slightly smaller than the other two equiaxed grains. This can be seen with the help of the dotted line in the figure. The marginally smaller size of the left hand grain nucleated by the 0.1 K inoculant is due to boundary effects.

These nucleated grains initially grow as equiaxed grains until the laterally growing arms impinge upon each other and stop further growth. Moreover, the columnar grains growing from the bottom prevent the arms of the equiaxed grains growing in the -Y direction. The arms of the equiaxed grains growing in the +Y direction continue to grow which is facilitated by the presence of the thermal gradient along the Y-axis. Thus, there is a tendency for the nucleated grains to grow in a columnar fashion after initial equiaxed growth.

At the higher cooling rate condition of 100 Ks^{-1} (Figure 2b), all five inoculants are activated, indicating that ΔT_n of 2 K was reached for the right hand most inoculant. As in the previous case, the right most grain is slightly smaller than the previous four grains. In this case also, the newly nucleated grains grow in an equiaxed manner in the initial stages which later tend to grow in a columnar fashion following the thermal gradient. Nucleated inoculants showing elongated growth have also been obtained by Badillo-Beckermann [30] in their numerical analysis. Note that their work placed multiple rows of inoculants ahead of the growing columnar grains as opposed to one row of inoculants in the current work. Furthermore, their work also shows an increased number of nucleation events with increasing $\dot{T}$ (pull rate). Additionally, recent directional solidification experiments on Al-20%Cu confirm the elongated growth of the equiaxed grains aligned with the temperature gradient [60].

3.2 Medium and high temperature gradients:

Figure 3 (a-f) shows the results for simulations for 'medium' and 'high' G - 1000 Km^{-1} and 10000 Km^{-1} in the upper and lower rows respectively. Results from the six conditions are presented in three columns, with each column representing a given $\dot{T}$ - the left most column represents results for 1 Ks^{-1} which increases to 100 Ks^{-1} for the right most column. As G increases, the number of nucleation events reduces for the low cooling rate condition of 1 Ks^{-1}. On the other hand, at higher cooling rates all five inoculants are activated irrespective of

the thermal gradient. However, additional simulations showed that for higher $\dot{T}$ cases of up to 100 Ks^{-1}, the inoculants may be deactivated at G values of 500000 Km^{-1} or higher. At lower G values of 100000 Km^{-1}, even lower $\dot{T}$ cases of 1 or 10 Ks^{-1} did not activate all the inoculants. Note that for all cases the images are shown only for a limited simulation time. The complete simulation time shows inoculated grains eventually assume a columnar morphology. The solidification behaviour of each G and $\dot{T}$ combination is described as follows.

G - 1000 [Km^{-1}]; $\dot{T}$ - 1 [Ks^{-1}] (Figure 3a): All twenty epitaxially nucleated columnar grains grow and activate nucleation on four inoculants but not on the inoculant with the highest ΔT_n of 2.0 K. The columnar grains are largely cellular growing in the direction of the temperature gradient (from lower to higher temperature). The nucleated grains initially grow equiaxially with a dendritic morphology. With time, the primary arm that lies parallel to the temperature gradient grows faster than the other three arms.

G – 1000 [Km^{-1}]; $\dot{T}$ - 10 [Ks^{-1}] (Figure 3b): In this case, the bottom twenty grains grow with a morphology that has a more dendritic structure, with secondary arms growing from the individual grains. All five inoculants are activated and the grains subsequently grow as dendritic equiaxed grains.

G – 1000 [Km^{-1}]; $\dot{T}$ - 100 [Ks^{-1}] (Figure 3c): As $\dot{T}$ increases further, the bottom columnar grains tend to become more dendritic. As in the previous case, all five inoculants are activated, and these grains grow with an equiaxed morphology.

G – 10,000 [Km^{-1}]; $\dot{T}$ - 1 [Ks^{-1}] (Figure 3d): All twenty columnar grains grow with a mixture of cellular-dendritic morphologies. Three inoculants are activated (0.1, 0.2, 0.5 K) which

subsequently start to grow with an equiaxed structure. The morphology of the equiaxed grains is similar to that of the previous case with the same $\dot{T}$ but a lower G.

G – 10,000 [Km^{-1}]; $\dot{T}$ - 10 [Ks^{-1}] (Figure 3e): Same result as $G1000\dot{T}10/\dot{T}100$ reported above with all five inoculants activated and the bottom twenty grains grow with a dendritic morphology.

G – 10,000 [Km^{-1}]; $\dot{T}$ - 100 [Ks^{-1}] (Figure 3f): Same result is observed as for $G10000\dot{T}10$.

4. Discussion

Salient features of the results are as follows:

- At lower cooling rates the increasing thermal gradient inhibits nucleation. This is well known and has been proposed previously ([25]).
- Higher cooling rates (10-100 Ks^{-1}) result in nucleation on all inoculants which suggests higher available undercooling. In X-ray synchrotron experiments with varying cooling rates in the Al-Cu system, Liotti et al have recently showed that increasing the cooling rate increases the number of nucleation events in the solidifying systems [61]. Similarly, the in-situ directional solidification experiments by Xu et al on binary Al-Cu alloys also show increased nucleation with increasing cooling rates [60, 62].

The following analysis of the observed results use the framework of the Interdependence Model which is based upon nucleation occurring on substrates of a given ΔT_n facilitated by ΔT_{CS} attained ahead of an already growing grain due to the rejected solute [32].

4.1 Theoretical Considerations

The Interdependence Model is based on *CS* being generated ahead of the growing interface due to solute rejected from the interface of an already nucleated and growing grain [32].

Figure 4 schematically describes, using the framework of the Interdependence Model, how high thermal gradients and cooling rates affect nucleation and the grain size. This schematic is to assist the interpretation of the model results presented subsequently. The Interdependence Model proposes that the grain size, *d*, is the sum of three components, i.e.

$$d = x_{cs} + x'_{dl} + x_{sd} \quad (1a)$$

which is based on the following analytical equation

$$d = \frac{D_l z \Delta T_n}{vQ} + \frac{4.6 D_l}{v}\left(\frac{c_l^* - c_0}{c_l^*(1-k_e)}\right) + x_{sd} \quad (1b)$$

where x_{cs} is the amount of growth a grain must undertake to generate sufficient ΔT_{CS} required for nucleation, x'_{dl} is the length of the solute diffusion zone to the point of maximum ΔT_{CS}, and x_{sd} is the average distance to the next available nucleant. D_l is the diffusivity of the solute elements in the liquid, v is the growth velocity, ΔT_n is the nucleation undercooling, Q $(= mc_0(k_e - 1))$ is the growth restriction factor (~5.6 K for Al-2Cu [63]), c_l^* is the composition of the liquid at the dendrite tip, c_0 is the alloy composition, and k_e is the equilibrium partition coefficient. Originally, the Interdependence Model assumed a low thermal gradient in the melt. The z term in equation 1b is a *CS* re-generation term that incorporates the thermal gradient [32].

Figures 4 a & b contrast two extremes of the solidification conditions investigated here: low *G* low $\dot{T}$ (for example *G*500$\dot{T}$0.25) and high *G* high $\dot{T}$ (for example *G*10000$\dot{T}$100). To understand the transient nature of the solidification process two times are considered. The

solid line is for some arbitrary initial time, t_0, and the dashed line is for a later time, t_1. The slope of the lines represents the thermal gradient ((a) low, and (b) high). The difference in the solid and the dashed lines is governed by the cooling rate ((a) low, and (b) high).

In both cases an undercooled zone is observed. With the low *G* low $\dot{T}$ case, the *CS* region is the sum of x_{cs} and x'_{dl}, both of which are considerably longer than in the high *G* high $\dot{T}$ case. This is due to the higher $\dot{T}$ leading to increased v (Eqn. 1). The other effect shown in Figure 4, which has not been previously considered in the Interdependence Model, is that an increased *G* causes the thermal liquidus isotherm to lead the dendrite growth and simultaneously, the propensity of the growth velocity (v in Eq. 1) to lag the thermal isotherm velocity (equal to the pull velocity v_{pull} in the simulations). This lag results in a significant contribution to the undercooling at high cooling rates and is thermally driven. These factors are further analysed using the data from the simulations.

4.2 Growth Velocity

The growth rate of the growing columnar grains was determined for all run conditions. Following the simulations, the interface position of the columnar grain (solid) aligned with the middle inoculant (# 3) was tracked as a function of time. Inoculant # 3 was chosen as it has the median ΔT_n for the simulation. Similar solute profiles ahead of the parallel growing columnar grains shown in the figures in Appendix B confirm that the middle inoculant may be used to analyse the results. The extent of the solid columnar grain was identified by the array of cells in the domain which displayed zero undercooling. The solid growth was therefore the difference in the 'solid' cell count from one time-stamp to the next. Since the cell size is known, the cell count provides the magnitude of the position of the solid-liquid interface, that is, the tip of the columnar grain. The rate of change of position with time is the tip growth rate. Note that a diffuse solid/liquid interface was modelled in the current

simulations based on the local solid fraction, where $f_s = 1$ represents a fully solid, and $f_s = 0$ represents a fully liquid cell. A solid fraction of 0.5 for the local cell (size 2 μm) was used to identify the cell as solid-liquid interface.

The locus of the tip showed a non-linear correlation with time for all conditions suggesting a changing tip growth rate. Figure 5 shows a typical plot for the $G10000\dot{T}1$ case for the columnar grain aligned with inoculant #3. Figure 5a shows the position of the tip as a function of solidification normalised time (until nucleation is triggered) with a fitted power law. Figure 5b shows the tip growth rate to vary non-linearly as a function of undercooling. Tip velocity in constitutionally driven growth is expected to follow a non-linear power law with respect to the undercooling when the undercooling is small [46]. As seen in Figure 5b the *μMatIC* model retrieves this feature. Recall that the current model dynamically calculates the tip growth rate and no power law is assigned *a priori*.

An average tip growth velocity can be calculated in the case of a non-linear correlation as seen in the present case using the standard definition of an average quantity $v_{avg} = \frac{\Delta L}{\Delta t}$, where ΔL is the total displacement and Δt is the time required for the total displacement [64]. The elapsed time Δt was taken from the time the growth of the columnar grains began, to the time when the inoculant activated a nucleation event ahead of the growing interface. The growth rates are presented in Table 3. Note that the estimated growth rate from experiments has shown that the tip growth-rates of equiaxed grains during X-ray synchrotron experiments fall in a wide range of a few tens to a few hundreds of microns per second [64, 65]. Although the current estimate is for columnar growth, the results seem reasonable.

For a given thermal gradient, the average growth rate increases with increasing cooling rate. This is expected as $\dot{T}$ is directly proportional to the pull rate ($\dot{T} = G.v_{pull}$). Although this is

the case, the ratio of the average growth rate, v_{avg}, to the pull rate, v_{pull}, decreases with increasing $\dot{T}$ for a given thermal gradient. This suggests that the estimated v_{avg} lags the imposed v_{pull} and this lag increases considerably with increasing $\dot{T}$. This lag was confirmed by the locus of the liquidus isotherm which followed the pull velocity. In addition, the higher propensity for dendritic growth of the columnar grains at higher cooling rates (Figures 2b, 3c, and 3f) also suggests a lower tip growth, v_{avg}, translating as a greater lag with v_{pull}. Even though the ratio presented in column 4 in Table 3 is based on simulations for equilibrium conditions and may vary from reality, the lag of v_{avg} behind v_{pull}itself is very significant.

Table 3. Comparison of growth rates for the columnar grains obtained from pull rate and the actual simulation. The linear growth rate equation for the simulations suggests a constant growth rate.

Run	v_{avg} **[µm/s]**	v_{pull} **[µm/s]**	$\frac{v_{avg}}{v_{pull}}$ **[%]**
$G500\dot{T}0.25$	19.2	500	4
$G500\dot{T}100$	364	200000	0.2
$G1000\dot{T}1$	36.6	1000	3.7
$G1000\dot{T}10$	85.7	10000	0.9
$G1000\dot{T}100$	285.7	100000	0.3
$G10000\dot{T}1$	37.6	100	37.6
$G10000\dot{T}10$	168	1000	16.8
$G10000\dot{T}100$	400	10000	4

It has been proposed that the higher cooling rates and associated rapid solidification conditions during AM lend themselves to solute trapping with reduced partitioning [47]. The

current simulations assume equilibrium solidification conditions. Given that the estimated growth rates for all conditions are well below the rates that would categorize them as rapidly solidified (0.1 – 5 m/s, [66]), the current approach will provide a good understanding of the mechanisms occurring even if there is some deviation from the exact prediction.

To summarise, the growth velocity, *v*, is influenced by the solidification conditions in the following ways

- High $\dot{T}$ increases v_{avg} substantially. This will reduce x_{cs} and x'_{dl} (Equation 1 & Figure 4). Note that v_{avg} from the simulation corresponds to v in Eqn. 1b.
- v_{avg} lags v_{pull} substantially, particularly at high $\dot{T}$. The lag with distance appears to be smaller at high *G*. This results in an extra contribution to the undercooling which is greater with high *G* (Figure 4). Thus, the total undercooling is made up of ΔT_{CS} and ΔT_{therm}, neglecting the attachment kinetics and the small contribution from the curvature undercooling ($\Delta T_{total} = \Delta T_{CS} + \Delta T_{therm}$).

4.3 Solute profile

To clarify the role of solute and its interplay with the thermal gradient in establishing the required undercooling, the solute profile ahead of the growing columnar grains was also analysed. As a first step in this analysis it was determined whether there was a difference in the solute profile ahead of different columnar grains. Following Figure B1 the analysis presented in the following is for the middle columnar grain with inoculant #3 (0.5 K) placed ahead of it, unless stated otherwise.

The time dependent solute concentration and the associated total undercooling was extracted from the simulations. Here the total undercooling is the available undercooling which changes with time as discussed in Figure 4. Figures 6 and 7 show the simulation results for

*G*500, *G*1000 and *G*10000 series at different cooling rates. The low solute concentration shown to the left of the interface is that of the solid phase. The interface advances with time and the length of this solid phase zone represents x_{cs} in Eqn. 1. The solute concentration and the total undercooling in the liquid are plotted as a function of the distance ahead of the growing columnar grains along the growth direction. Note that the range of undercooling and solute curves were chosen such that they represent the time-stamps ranging from when some initial columnar growth had taken place until a nucleation event was first activated on inoculant #3. Four time-stamps were selected in this range which are numbered 1 to 4 and are presented as a family of curves. Curve 1 corresponds to the time at the start of columnar growth and curve 4 corresponds to the time when nucleation on inoculant #3 first occurs. The simulation time corresponding to t_4 is provided in the figures, and is lower for faster cooling rates.

In Figure 6a, as the solidification time proceeds, the amount of solute rejected ahead of the interface (solid grain is where c_l < 2) increases with a corresponding increase in the total undercooling, almost entirely provided by ΔT_{CS}. At a distance of 200 μm, where the inoculant is placed, a nucleation event occurs when the undercooling reaches 0.5 K. For this low *G* and $\dot{T}$ case, x_{cs} is ~50 μm and x'_{dl} is ~150 μm when 0.5 K undercooling is attained (curve 4). Thus, solutal undercooling (*CS*) is established quite early as indicated by the early nucleation and growth of equiaxed grains in Figure 2a (also 3a and 3d). The sum of $x_{cs} + x'_{dl}$ is termed the nucleation free zone (NFZ) [32]. Since the interface concentration increases with growth of the columnar grain, the available *CS* also increases with time and contributes to the total undercooling, ΔT_{total}. However, no nucleation is possible until the available *CS* equals ΔT_n ($\Delta T_{CS} = \Delta T_n$). The growing grain ($x_{cs}$) and the increasing diffusion length (x'_{dl}) continuously changes the NFZ. At t_4 when 0.5 K undercooling is reached the NFZ is ~200 μm. At this time, the tip concentration, c_l^*, is ~2.2 which translates to ΔT_{CS} = 0.52 (using $m(c_l^* - c_0)$).

Note that at a distance of 150 μm, the positive thermal gradient consumes 0.075 K of this undercooling. This suggests that the *CS* provides for practically all of the undercooling, ΔT_{total}, required for nucleation.

The solute profile for the columnar grain corresponding to the last inoculant with ΔT_n of 2 K is shown in Figure 6b ($\dot{T}$0.25). Recall from Figure 2a that no nucleation event occurred in this case. As in Figure 6a, the solute content at the interface, c_l^*, increases with time, with a corresponding increase in ΔT_{CS}. The maximum total undercooling obtained is ~0.8 K at time-stamp t_3 with ΔT_{CS} = 0.78 K, corresponding to c_l^* of ~2.3. Once again, *CS* contributes to practically all of the total undercooling, ΔT_{total}. Clearly, both the total undercooling, ΔT_{total}, and the *CS*, ΔT_{CS}, are well below the 2 K required for nucleation and no nucleation is observed. Curve 4 in Figure 6b represents the growth of the columnar grain up to 200 μm where the inoculants are placed. ΔT_{CS} would have also increased with time, however it never reaches 2 K and consequently no nucleation event is activated.

The faster cooling rate case in Figure 6c (G500$\dot{T}$100) shows a contrasting result. As time progresses, the peak solute content ahead of the advancing interface quickly rises to a similar, though a lower value, to that of the lower cooling rate case. However, the solute gradient increases with increasing cooling rate and the solute reaches the nominal composition very quickly relative to slower cooling rates. This is expected as the solute gradient increases with increasing tip velocity (see Table 3). When x_{cs} increases in Equation 1 and Figure 4, x'_{dl} decreases, which means that the NFZ or the length of the boundary layer of varying solute reduces dramatically at the higher cooling rates. In this case, the NFZ is significantly reduced and is barely a few tens of microns in length.

On the other hand, it is observed that while both *CS*, ΔT_{CS}, and the total undercooling, ΔT_{total}, increase with the advancing interface, ΔT_{total} increases much faster than ΔT_{CS} at high cooling rates compared to the low cooling rate case. For example, for t_4, where c_l^* is ~2.25 at the interface which has grown ~10 μm, ΔT_{CS} = 0.65 K and ΔT_{total} is ~2.2 K. Such a high undercooling enables ΔT_n of 2 K to be reached and triggers nucleation 190 μm away from the S-L interface. Note that the positive thermal gradient (500 Km^{-1}) consumes 0.1 K of this total undercooling. After further subtracting ΔT_{CS} = 0.65 K from the remainder, an undercooling of 1.45 K remains. This additional undercooling on top of ΔT_{CS} is attributed to the lag in tip growth rate, v_{avg}, compared to the pull rate, v_{pull}. This undercooling may be termed $\dot{T}$-induced thermal undercooling, $\Delta T_{CR\text{-}therm}$, hereafter. For the higher $\dot{T}$ case discussed for time stamp t_4 in Figure 6c, $\Delta T_{CR\text{-}therm}$ = 1.45 K which is much larger than ΔT_{CS} = 0.65 K and accounts for the majority of the total undercooling required to activate inoculant # 5 at higher cooling rates. The role of the lag between v_{avg} and v_{pull} in contributing to the total undercooling is also shown schematically in Figure 4c.

Interestingly, the directional solidification results by Xu et al [60] show that the nucleation front velocity follows the theoretical pull rate suggesting that the available undercooling for nucleation is a function of the pull rate. In addition, they also estimated the maximum available undercooling to be in the range of ~0.5 K to ~3 K, with undercooling increasing with increasing cooling rate [62]. The available undercooling was found to be strongly dependent upon the cooling rate. As such, the notion of $\Delta T_{CR\text{-}therm}$ induced as a result of the difference between v_{pull} and v_{avg} is reasonable.

For the higher thermal gradient (*G*1000 series) similar results are observed (Figure 7 a-c). For $\dot{T}1$ (Figure 7a) the solute concentration ahead of the advancing interface increases with time with a corresponding increase in the magnitude of undercooling with time. In addition, the

undercooling curves also follow the thermal gradient, resulting in parallel slopes for the undercooling curves (particularly at higher $\dot{T}$ when the NFZ is small). That is, the undercooling is influenced by both the solute profile (x'_{dl}) as well as the thermal gradient (G). For $\dot{T}10$ (Figure 7b) and $\dot{T}100$ (Figure 7c), the solute content reaches the nominal composition very quickly (quicker for $\dot{T}100$ as x_{cs} is smaller) and stays constant with increasing time, but the magnitude of undercooling continues to increase with time which therefore also suggests the contribution of $\Delta T_{CR\text{-}therm}$. This result is similar to that with the highest cooling rate for the $G500$ case (Figure 6c). In Figures 6c and 7c, the tip temperature would be higher (corresponding to lower c_l^*) due to the higher thermal gradient, G. But, higher $\dot{T}$ reduces the temperature quickly resulting in $\Delta T_{CR\text{-}therm}$.

As in the previous two cases, the $G10000$ series results (Figure 7 d-f) also show an increase in the absolute value of undercooling with time which activates nucleation. The effect of solute in establishing the undercooling is clearly seen in Figure 7d. Figures 7e and f show the parallel profiles of the family of undercooling curves demonstrating the role of cooling rate in generating undercooling as x'_{dl} reduces with increasing $\dot{T}$. There seems to be solute driven growth in Figure 7d as seen by the larger growth of the columnar grains (marked by curly brackets in the figure). On the other hand, at the highest $\dot{T}$ (Figure 7f) the undercooling is almost entirely controlled by cooling rate with negligible columnar growth as seen in Figures 6c and 7c.

Figure 8 summarizes the relative contribution of constitutional supercooling, ΔT_{CS}, and cooling rate induced thermal undercooling, $\Delta T_{CR\text{-}therm,}$ to the total undercooling, ΔT_{total}, available for nucleation at different cooling rates for $G10000$. When $\dot{T}$ increases from 1 Ks^{-1} to 100 Ks^{-1}, the fraction of $\Delta T_{CR\text{-}therm}$ increases from 7% to 75%. This is mitigated to a small

extent by an increase in thermal gradient. These results are consistent with the more substantial lag of tip growth behind the isotherm when cooling rate increases.

Recall from Figures 2 and 3 that under low $\dot{T}$ the number of nucleation events activated were fewer than for higher $\dot{T}$. The simulation results show that the undercooling generated was insufficient at lower $\dot{T}$. On the other hand, at the highest cooling rates, the greatest contribution to the undercooling is a result of the cooling rate. For small to medium cooling rates (~10 Ks^{-1}), the undercooling that activates a nucleation event is governed largely by the solute. For higher cooling rates, as one would expect in AM processes, the undercooling generated by the cooling rate is dominant, although the undercooling profile still follows the thermal gradient. Therefore, for higher cooling rates, solute has a lesser role in establishing the required undercooling but is still critical in generating the initial undercooling in front of the interface. Thus, there appears to be a transition from solute-controlled to $\dot{T}$*-induced* undercooling ($\Delta T_{CR\text{-}therm}$).

Closely following the Gaumann, Trivedi, and Kurz (GTK) model [67], Quested and Greer (Figure 1 in [68]) show similar results as seen in this work, namely, a dominating solutal undercooling (*CS*) for slower tip growth rates. However, at higher tip growth rates (equivalent to the high $\dot{T}$ condition in μ*MatIC* simulations), Quested and Greer [68] equate the available undercooling ahead of the dendrite tip with purely solutal undercooling, which is higher than for the lower tip growth rates. This is because the GTK model neglects thermal undercooling due to the assumption of high thermal diffusivity. The numerical model used in the current work utilizes thermal diffusion as well as solutal diffusion. The current results can therefore be explained on the basis of thermal undercooling.

Finally, it is interesting to note that Badillo and Beckermann [30] observed a solute pile-up effect between nucleated equiaxed grains with inoculants spaced at <50 μm. In the present

case, the inoculants were placed at 200 μm spacing and no evidence of solute-pile up was observed at this large spacing for the solidification times studied. The *μMatIC* model has also shown evidence for solute pile-up previously [54].

4.4 Interdependence Model

The Interdependence Model explains the observed results in that a minimum required undercooling (ΔT_n) needs to be established to activate a nucleation event. In terms of the Interdependence Model, increasing $\dot{T}$ reduces the diffusion length (shown as x'_{dl} in Figure 4) which severely reduces the size of the Nucleation free zone (NFZ) as can be seen in Figures 6c, 7c, and 7f. This implies that in AM processes where high G and $\dot{T}$ conditions are likely to be encountered, the nucleation events can be expected to be via $\dot{T}$-induced thermal undercooling ($\Delta T_{CR\text{-}therm}$) resulting in reduced grain size. In such cases, it is suggested that the solute would have a relatively lesser effect on grain size than in conventional casting.

Results from in-house laser surface remelting (LSR) experiments on grain refined and unrefined Al-2, 5, 7 Cu and Si alloys were compared with the result from as-cast solidification experiments (Al-Cu results have been presented in [69]). The experimental results are presented in Figure 9 ((a-d) microstructures and (e & f) Grain size – 1/Q plot) [69]. A plot of grain size as a function of 1/Q shows that the effectiveness of the inoculant particles increase dramatically in the grain refined LSR samples (reduced intercept) and the NFZ is almost eliminated (reduced gradient) [33]. It is known that in as-cast alloys only about 1% of particles become activated nucleants [70]. In the case of the results shown here the proportion of TiB_2 particles increased from approximately 0.1% to >20% [69] that were activated during laser remelting, indicating that the high cooling rate in AM can generate very large undercooling to enable the smaller TiB_2 particles to become active nucleants. Furthermore, the Al-Si data shows that even when the as-cast grain size results show the well-known Si-

poisoning effect, significant refinement is seen in the LSR Al-Si alloys. Discussion of the Si-poisoning mechanisms is beyond the scope of the current work.

It is of interest to predict the effect of very high cooling rates during the AM processes from the perspective of the Interdependence Model. The implication of non-equilibrium solidification conditions due to high cooling rates is that the NFZ would tend to decrease on two counts – 1) higher growth rates of the tip (first two terms in Eqn.1), and 2) decreased *CS* due to possible solute trapping (second term in Eqn. 1). While *CS* was shown to be a driving force for nucleation at low cooling rates, the $\Delta T_{CR\text{-}therm}$ contributes more significantly at higher cooling rates. As such, the loss in *CS* may not be a hindrance to activating nucleation events. These may be verified using a modified *μMatIC* model where non-equilibrium conditions have been incorporated.

5. Conclusions

1. The *μMatIC* solidification model was used to simulate equiaxed grain nucleation under a range of cooling rates in the presence of low, medium and high thermal gradients. Inoculants of known undercooling were placed ahead of the growing columnar grains which were activated during solidification depending upon the cooling conditions. In general, a higher temperature gradient reduced the number of nucleation events, while higher cooling rates increased the number of events.
2. According to analysis using the Interdependence Model there are three ways that high cooling rates and thermal gradients can affect the CET and grain size. One is that there is an increase in solidification rate which leads to a reduction in the size of the nucleation free zone until it is almost negligible. The second is that an increase in thermal gradient can reduce the amount of constitutional supercooling in front of the interface which can lead to columnar grain growth. The third effect, and what appears

to be the most significant effect at the very high cooling rates is that the growth of the dendrites substantially lags the pull velocity leading to an undercooled zone being formed between the solid-liquid interface and the point of thermal equilibrium.

3. It was shown that the principles of the Interdependence Model can be used in CET studies with columnar growth activating equiaxed nucleation and growth. The nucleation results can be explained on the basis of the undercooling required to activate a nucleation event.
4. While ΔT_{CS} was active at all cooling rates, at low and medium cooling rates (up to ~10 Ks^{-1}) it was the dominant contributor to undercooling. At higher cooling rates there was a transition to $\dot{T}$-induced thermal undercooling (termed $\Delta T_{CR\text{-}therm}$) which was the major contributor to the undercooling required for activating nucleation.

Declaration of interests

The authors declare that they have no known competing financial interests or personal relationships that could have appeared to influence the work reported in this paper.

Acknowledgements:

The authors would like to acknowledge the support provided by ARC Discovery grant DP160100560. The staff and facilities of the RMIT Advanced Manufacturing Precinct are acknowledged for the laser surface remelting experiments and the RMIT Microscopy and Microanalysis Facility is acknowledged for the microstructural characterisation.

References:

[1] J.J. Lewandowski, M. Seifi, Metal Additive Manufacturing: A Review of Mechanical Properties, Annual Review of Materials Research 46 (2016) 151-186.
[2] T.S. Srivatsan, T.S. Sudarshan, Additive Manufacturing: Innovations, Advances, and Applications, CRC Press, 2016.
[3] A.E. Ares, C.E. Schvezov, Influence of Solidification Thermal Parameters on the Columnar-to-Equiaxed Transition of Aluminum-Zinc and Zinc-Aluminum Alloys, Metallurgical and Materials Transactions A 38 (2007) 1485-1499.
[4] J. Mazumder, A. Kar, One-dimensional diffusion model for extended solid solution in laser cladding, Journal of Applied Physics 61 (1987) 2645-2655.
[5] J.W. Elmer, S.M. Allen, T.W. Eagar, Microstructural Development during Solidification of Stainless Steel Alloys, Metallurgical and Materials Transactions A 20 (1989) 2117-2131.
[6] J. Mazumder, A. Schifferer, J. Choi, Direct materials deposition: designed macro and microstructure, Materials Research Innovation 3(3) (1999) 118-131.
[7] M.L. Griffith, M.E. Schlienger, L.D. Harwell, M.T. Ensza, M. Essiena, J. Brooks, M.S. Olivera, W.H. Hofmeister, M.J. Wert, D.V. Nelson, C.V. Robino, J.E. Smugeresky, M.D. Baldwin, Understanding thermal behavior in the LENS process, Materials and Design 20 (1999) 107-113.
[8] W. Hofmeister, M. Griffith, M. Ensz, J. Smugeresky, Solidification in Direct Metal Deposition by LENS Processing, Journal of Metals (2001) 30-34.
[9] P.A. Kobryn, S.L. Semiatin, Microstructure and texture evolution during solidification processing of Ti–6Al–4V, Journal of Materials Processing Technology 135 (2003) 330-339.
[10] L. Qian, J. Mei, J. Liang, X. Wu, Influence of position and laser power on thermal history and microstructure of direct laser fabricated Ti–6Al–4V samples, Materials Science & Technology 21(3) (2005) 299-305.
[11] M. Doubenskaia, P. Bertrand, I. Smurov, Pyrometry in laser surface treatment, Surface & Coatings Technology 201 (2006) 1955–1961.
[12] R. Rai, J.W. Elmer, T.A. Palmer, T. DebRoy, Heat transfer and fluid flow during keyhole mode laser welding of tantalum, Ti–6Al–4V, 304L stainless steel and vanadium, Journal of Physics D: Applied Physics 40 (2007) 5753-5766.
[13] H. Tan, J. Chen, L. Xin, F. Zhang, W. Huang, Research on molten pool temperature in the process of laser rapid forming, Journal of Materials Processing Technology 198 (2008) 454-462.
[14] S.S. Al-Bermani, M.L. Blackmore, W. Zhang, I. Todd, The Origin of Microstructural Diversity, Texture, and Mechanical Properties in Electron Beam Melted Ti-6Al-4V, Metallurgical and Materials Transactions A 41 (2010) 3422-3434.
[15] T. Vilaro, C. Colin, J.D. Bartout, As-Fabricated and Heat-Treated Microstructures of the Ti-6Al-4V Alloy Processed by Selective Laser Melting, Metallurgical and Materials Transactions A 42A (2011) 3190-3199.
[16] J.J. Blecher, T.A. Palmer, T. Debroy, Solidification Map of a Nickel-Base Alloy, Metallurgical and Materials Transactions A 45 (2014) 2142-2151.
[17] M.H. Farshidianfar, A. Khajepour, A.P. Gerlich, Effect of real-time cooling rate on microstructure in Laser Additive Manufacturing, Journal of Materials Processing Technology 231 (2016) 468–478.
[18] U.S. Bertoli, G. Guss, S. Wu, M.J. Matthews, J.M. Schoenung, In-situ characterization of laser-powder interaction and cooling rates through high-speed imaging of powder bed fusion additive manufacturing, Materials and Design 135 (2017) 385-396.

[19] W. Ou, T. Mukherjee, G.L. Knapp, Y. Wei, T. DebRoy, Fusion zone geometries, cooling rates and solidification parameters during wire arc additive manufacturing, International Journal of Heat and Mass Transfer 127 (2018) 1084-1094.
[20] S.M. Kelly, S.L. Kempe, Microstructural Evolution in Laser-Deposited Multilayer Ti-6Al-4V Builds: Part I. Microstructural Characterization, Metallurgical and Materials Transactions A 35A(June) (2004) 1861-1867.
[21] R. Li, J. Li, Y. Shi, M. Du, Z. Xie, 316L Stainless Steel with Gradient Porosity Fabricated by Selective Laser Melting, Journal of Materials Engineering and Performance 19(5) (2010) 666-671.
[22] S. Wen, S. Li, Q. Wei, Y. Chunze, S. Zhang, Y. Shi, Effect of molten pool boundaries on the mechanical properties ofselective laser melting parts, Journal of Materials Processing Technology 214 (2014) 2660–2667.
[23] X. Zhao, Q. Wei, B. Song, Y. Liu, X. Luo, S. Wen, Y. Shi, Fabrication and Characterization of AISI 420 Stainless Steel Using Selective Laser Melting, Materials and Manufacturing Processes 30 (2015) 1283–1289.
[24] F. Yan, W. Xiong, E. Faierson, Grain Structure Control of Additively Manufactured Metallic Materials, Materials 10, 1260 (2017) 1-11.
[25] J.D. Hunt, Steady State Columnar and Equiaxed Growth of Dendrites and Eutectic, Materials Science and Engineering 65 (1984) 75-83.
[26] C.Y. Wang, C. Beckermann, Equiaxed Dendritic Solidification with Convection Part I. Multiscale/Multiphase Modeling, Metallurgical and Materials Transactions A 27 (1996) 2754-2764.
[27] C.-A. Gandin, From Constrained To Unconstrained Growth During Directional Solidification, Acta Materialia 48 (2000) 2483-2501.
[28] M.A. Martorano, C. Beckermann, Ch-A. Gandin, A Solutal Interaction Mechanism for the Columnar-to-Equiaxed Transition in Alloy Solidification, Metallurgical and Materials Transactions A 34(August) (2003) 1657-1674.
[29] H.B. Dong, P.D. Lee, Simulation of the columnar-to-equiaxed transition in directionally solidified Al-Cu alloys, Acta Materialia 53 (2005) 659-668.
[30] A. Badillo, C. Beckermann, Phase-field simulation of the columnar-to-equiaxed transition in alloy solidification, Acta Materialia 54 (2006) 2015-2026.
[31] C.-A. Gandin, Experimental Study of the Transition from Constrained to Unconstrained Growth during Directional Solidification, ISIJ International 40(10) (2000) 971-979.
[32] D.H. StJohn, M. Qian, M.A. Easton, P. Cao, The Interdependence Theory: The relationship between grain formation and nucleant selection, Acta Materialia 59 (2011) 4907–4921.
[33] M. Easton, D. StJohn, An analysis of the relationship between grain size, solute content, and the potency and number density of nucleant particles, Metallurgical and Materials Transactions A 36A (2005) 1911-1920.
[34] X. Li, W. Tan, Numerical investigation of effects of nucleation mechanisms on grain structure in metal additive manufacturing, Computational Materials Science 153 (2018) 159-169.
[35] L. Pengwei, W. Zhuo, X. Yaohong, M.F. Horstemeyer, C. Xiangyang, C. Lei, Insight into the mechanisms of columnar to equiaxed grain transition during metallic additive manufacturing, Additive Manufacturing 26 (2019) 22-29.
[36] P.A. Kobryn, S.L. Semiatin, The Laser Additive Manufacture of Ti-6Al-4V, Journal of Metals (2001) 40-42.
[37] S. Bontha, N.W. Klingbeil, P.A. Kobryn, H.L. Fraser, Effects of process variables and size-scale on solidification microstructure in beam-based fabrication of bulky 3D structures, Materials Science & Engineering A 513-514 (2009) 311-318.

[38] N. Raghavan, R. Dehoff, S. Pannala, S. Simunovic, M. Kirka, J. Turner, N. Carlson, S.S. Babu, Numerical modeling of heat-transfer and the influence of process parameters on tailoring the grain morphology of IN718 in electron beam additive manufacturing, Acta Materialia 112 (2016) 303-314.
[39] A. Plotkowski, M.M. Kirka, S.S. Babu, Verification and validation of a rapid heat transfer calculation methodology for transient melt pool solidification conditions in powder bed metal additive manufacturing, Additive Manufacturing 18 (2017) 256-268.
[40] M. Haines, A. Plotkowski, C.L. Fredericka, E.J. Schwalbach, S.S. Babu, A sensitivity analysis of the columnar-to-equiaxed transition for Ni-based superalloys in electron beam additive manufacturing, Computational Materials Science 155 (2018) 340-349.
[41] M.J. Bermingham, D.H. StJohn, J. Krynen, S. Tedman-Jones, M.S. Dargusch, Promoting the columnar to equiaxed transition and grain refinement of titanium alloys during additive manufacturing, Acta Materialia 168 (2019) 261-274.
[42] A. Hadadzadeh, B.S. Amirkhiz, J. Li, M. Mohammadi, Columnar to equiaxed transition during direct metal laser sintering of AlSi10Mg alloy: Effect of building direction, Additive Manufacturing 23 (2018) 121-131.
[43] F. Wang, S. Wang, P. Colegrove, A.A. Antonysamy, Microstructure and Mechanical Properties of Wire and Arc Additive Manufactured Ti-6Al-4V, Metallurgical and Materials Transactions A 44 (2013) 968-977.
[44] L. Bai, G. Le, X. Liu, J. Li, S. Xia, X. Li, Grain morphologies and microstructures of laser melting deposited V-5Cr-5Ti alloys, Journal of Alloys and Compounds 745 (2018) 716-724.
[45] S.N. Grigoriev, T.V. Tarasova, G.O. Gvozdeva, St. Nowotny, Solidification behaviour during laser microcladding of Al–Si alloys, Surface & Coatings Technology 268 (2015) 303-309.
[46] J.A. Dantzig, M. Rappaz, Solidification, EPFL Press2009.
[47] W.E. Frazier, Metal Additive Manufacturing: A Review, Journal of Materials Engineering and Performance 23 (2014) 1917-1928.
[48] P.D. Lee, J.D. Hunt, Hydrogen porosity in directionally solidified aluminium–copper alloys: a mathematical model, Acta Materialia 49 (2001) 1383-1398.
[49] R.C. Atwood, P.D. Lee, Simulation of the three-dimensional morphology of solidification porosity in an aluminium-silicon alloy, Acta Materialia 51 (2003) 5447-5466.
[50] W. Wang, P.D. Lee, M. McLean, A model of solidification microstructures in nickel-based superalloys: predicting primary dendrite spacing selection, Acta Materialia 51(2971-2987) (2003).
[51] H.B. Dong, P.D. Lee, Simulation of the columnar-to-equiaxed transition in directionally solidified Al–Cu alloys, Acta Materialia 53 (2005) 659-668.
[52] L. Yuan, P.D. Lee, Dendritic solidification under natural and forced convection in binary alloys: 2D versus 3D simulation, Modelling and Simulation in Materials Science and Engineering 18 (2010) 055008.
[53] L. Yuan, P.D. Lee, A new mechanism for freckle initiation based on microstructural level simulation, Acta Materialia 60(12) (2012) 4917-4926.
[54] A. Prasad, L.Yuan, P.D. Lee, D.H. Stjohn, The Interdependence model of grain nucleation: A numerical analysis of the Nucleation-Free Zone, Acta Materialia 61(16) (2013) 5914-5927.
[55] H.J. Dai, H.B. Dong, H.V. Atkinson, P.D. Lee, Simulation of the Columnar-to-Equiaxed Transition in Alloy Solidification -- the Effect of Nucleation Undercooling, Density of Nuclei in Bulk Liquid and Alloy Solidification Range on the Transition, Solid State Phenomena (2008) 7.

[56] A.L. Greer, Grain refinement of alloys by inoculation of melts, Philosophical Transactions of the Royal Society A: Mathematical, Physical, and Engineering Sciences 361 (2003) 479-495.
[57] M. Easton, D. StJohn, Grain Refinement of Aluminum Alloys: Part II. Confirmation of, and a Mechanism for, the Solute Paradigm, Metallurgical and Materials Transactions A 30A (1999) 1625-1633.
[58] C.Y. Wang, C. Beckermann, Equiaxed dendritic solidification with convection: Part II. Numerical simulations for an Al-4 Wt pct Cu alloy, Metallurgical and Materials Transactions A 27A (1996) 2765-2783.
[59] D.J. Fisher, W. Kurz, Fundamentals of Solidification, Trans-Tech Publications, Switzerland, 1998.
[60] Y.J. Xu, D. Caseri, R. H. Mathiesen, Y. Li, Revealing the heterogeneous nucleation behavior of equiaxed grains of inoculated Al alloys during directional solidification, Acta Materialia 149 (2018) 312-325.
[61] E. Liotti, C. Arteta, A. Zisserman, A. Lui, V. Lempitsky, P.S. Grant, Crystal nucleation in metallic alloys using x-ray radiography and machine learning, Science Advances 4 (2018).
[62] Y.J. Xu, D. Caseri, Q. Du, R.H. Mathiesen, L. Arnberg, Y.J. Li, Heterogeneous nucleation and grain growth of inoculated aluminium alloys: An integrated study by in-situ X-radiography and numerical modelling, Acta Materialia 140 (2017) 224-239.
[63] M. Johnsson, L. Backerud, The Influence of Composition on Equiaxed Crystal Growth Mechanisms and Grain Size in Al Alloys, Zeitschrift fur Metallkunde 87(3) (1996) 216-220.
[64] A. Prasad, S.D. McDonald, H. Yasuda, K. Nogita, D.H. StJohn, A real-time synchrotron X-ray study of primary phase nucleation and formation in hypoeutectic Al–Si alloys, Journal of Crystal Growth 430 (2015) 122-137.
[65] K. Nogita, H. Yasuda, A. Prasad, S.D. McDonald, T. Nagira, N. Nakatsuka, K. Uesugi, D.H. StJohn, Real time synchrotron X-ray observations of solidification in hypoeutectic Al–Si alloys, Materials Characterization 85 (2013) 134-140.
[66] J.H. Martin, B.D. Yahata, J.M. Hundley, J.A. Mayer, T.A. Schaedler, T.M. Pollock, 3D printing of high-strength aluminium alloys, Nature 549 (2017) 365-379.
[67] M. Gaumann, R. Trivedi, W. Kurz, Nucleation ahead of the advancing interface in directional solidification, Materials Science & Engineering A226-228 (1997) 763-769.
[68] T.E. Quested, A.L. Greer, Grain refinement of Al alloys: Mechanisms determining as-cast grain size in directional solidification, Acta Materialia 53 (2005) 4643-4653.
[69] M.N. Patel, D. Qiu, G. Wang, M.A. Gibson, A. Prasad, D.H. StJohn, M.A. Easton, Understanding the refinement of grains in laser surface remelted Al–Cu alloys, Scripta Materialia 178 (2020) 447-451.
[70] J.H. Perepezko, Metals Handbook, ASM, Metals Park, 1988, p. 101.

APPENDIX A: Test results from the modified *μMatIC* model

A 2-grain scenario was chosen to test the numerical model's ability to handle ΔT_n being assigned to individual inoculants. Figure A.1a shows the computational domain along with the two growing grains for this scenario with G being zero. The two grains were allowed to nucleate and grow from the alloy liquidus temperature. Figure A.1b shows the total undercooling ΔT_{CS} as a function of time at the mid-point between the two growing grains. The magnitude of ΔT_{CS} increases initially. However, with time, as the growing grains reject solute, there is solute pile up at the mid-point which starts to decrease the amount of ΔT_{CS} available. As such, the maximum possible ΔT_{CS} for this situation is slightly less than 0.2 K. Throughout this article, the values of undercooling (ΔT_n and ΔT_{CS}) are denoted with a positive sign. Thus, increased undercooling corresponds to more undercooling being available and vice versa.

The result in Figure A.1b provides an appropriate means to test the model for handling individual inoculants with different values of ΔT_n. An inoculant was placed at the mid-point of the two growing grains. Based on the constitutional supercooling seen in Figure A.1b, three cases were simulated where the mid-inoculant is assigned different values of ΔT_n: 0 K (i.e. at alloy liquidus), 0.1 K, and 0.2 K. A correctly functioning model would activate a nucleation event for the inoculant placed at the mid-point with undercoolings of 0 K and 0.1 K. On the other hand, no nucleation is expected for the inoculant of 0.2 K. These three cases are illustrated in Figure A1 c-e which shows the expected results from the three simulations. This confirms the functioning of the model with individual inoculants of specified ΔT_n.

APPENDIX B: Solute profile ahead of the growing columnar grains

The analysis presented was based on solute profile for the columnar grain aligned with inoculant # 3 (0.5 K). The following shows the validity of this approach. Figure B.1 shows the solute profiles ahead of columnar grains aligned with the five inoculants for two different run conditions ((a) $G1000\dot{T}1$ and (b) $G1000\dot{T}100$). There is some difference in the amount of grain growth of the inoculated grains in (a). However minimal difference is found in the solute profiles indicating that any of columnar grains could be selected for the analysis.

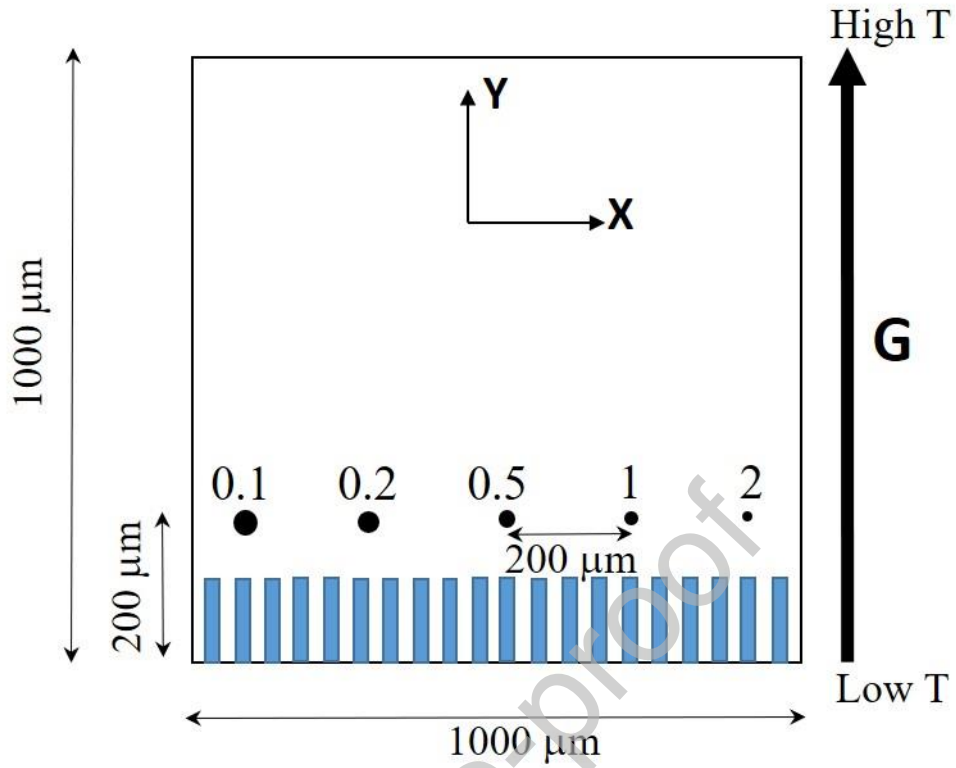

Figure 1: Computational domain to test the CET under a range of conditions for the Al-2Cu system. The gradient is imposed along the Y-axis as indicated. The assigned undercoolings are represented by the numbers 0.1 K to 2.0 K. The size of the inoculant reflects the undercooling (inoculant sizes not in proportion to the undercooling).

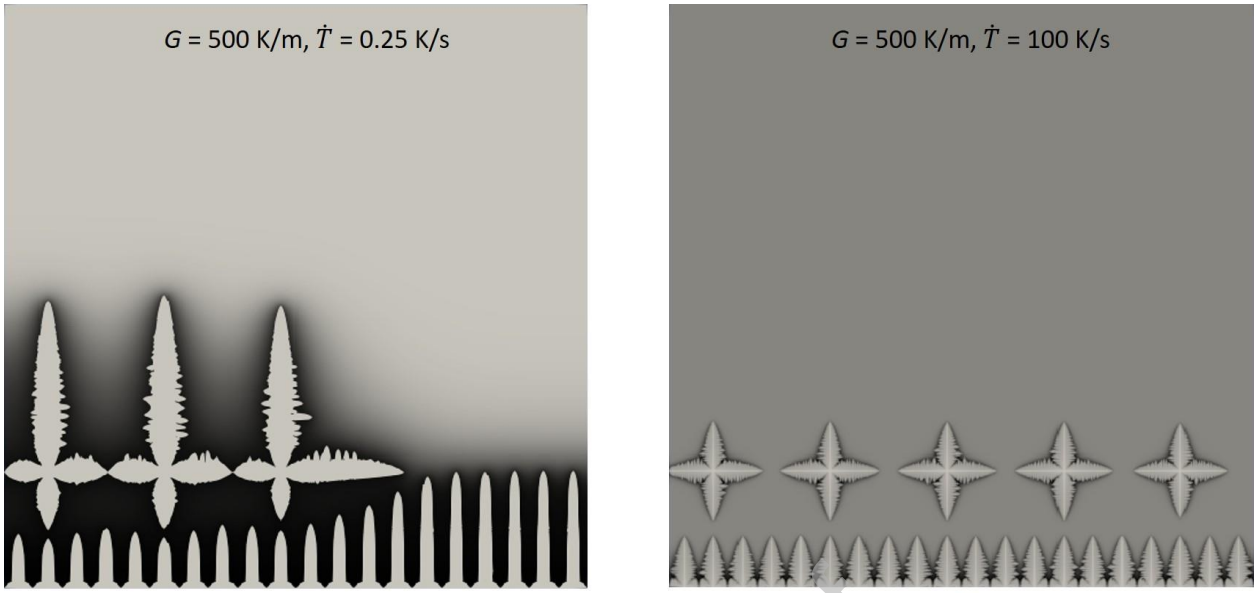

Figure 2: Results from the "Low" temperature gradient of G = 500 Km^{-1}. The bottom columnar grains grow with cellular morphology. **(a)** Only three equiaxed grains are activated (0.1 to 0.5 K undercooling) for the low cooling rate of 0.25 Ks^{-1}. **(b)** Increasing the cooling rate to 100 Ks^{-1} results in all five inoculants being triggered. The dotted lines help indicate the smaller size of the middle grain in (a) and the rightmost grain in (b).

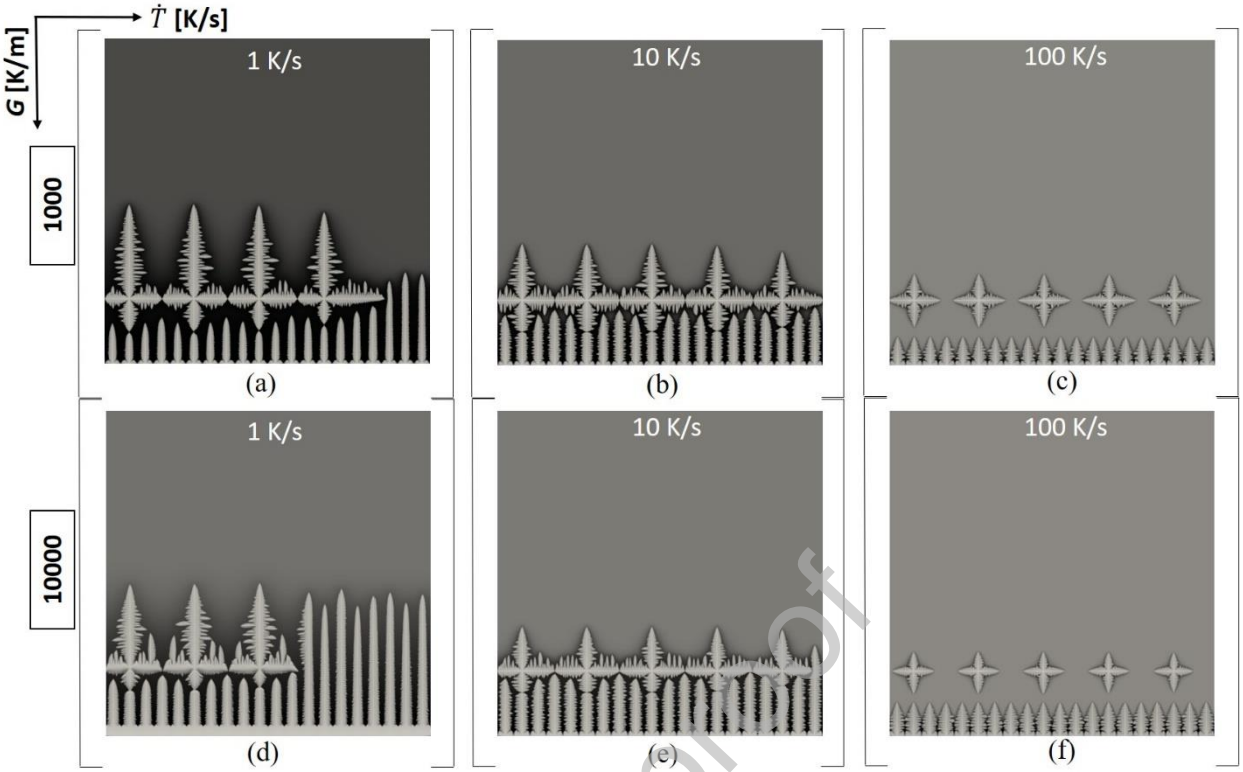

Figure 3: Simulation results for the "medium" and "high" temperature gradients under three $\dot{T}$ conditions.

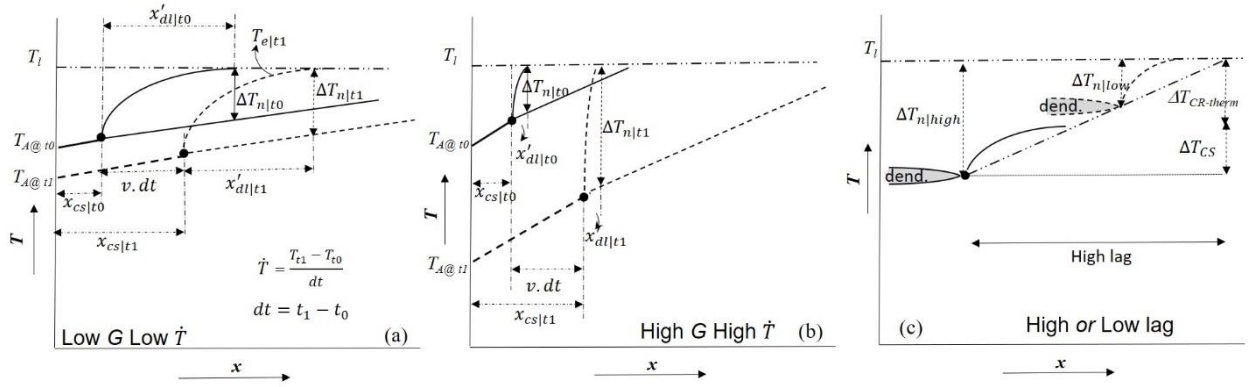

Figure 4: Temperature-distance schematic for **(a)** low G low $\dot{T}$, and **(b)** high G high $\dot{T}$ cases. The domain temperature T_A with a given thermal gradient is shown as a function of distance ahead of the advancing interface marked with a solid circle. The drop in temperature at arbitrary times t_0 and t_1 governed by the imposed cooling rate is shown by the difference between the solid and the dotted lines. The interface advances by $v.dt$ in a given time step, where v is the interface growth rate. The rejected solute from the growing S-L interface is converted into T_e using the alloy phase diagram plateauing to the liquidus, T_l, at the nominal alloy composition. The available undercooling for nucleation is denoted by ΔT_n which is a function of the thermal gradient, cooling rate and the interface growth rate. The correspondence with the Interdependence Model is shown with marked grain growth, x_{cs}, and diffusion length, x'_{dl}. While x_{cs} grows with time, x'_{dl} decreases as the $\dot{T}$ increases corresponding to a higher v at higher $\dot{T}$. At high G, *CS*-driven undercooling is small, but the undercooling is expected to increase due to the large fall in T_A under high $\dot{T}$. **(c)** shows the thermal undercooling available due to higher S-L interface lag at high $\dot{T}$ (solid) as compared to lower S-L interface lag (dotted). At high lag, the *CS* can provide only a fraction of the total undercooling. The remainder is the cooling rate induced thermal undercooling, $\Delta T_{CR\text{-}therm}$.

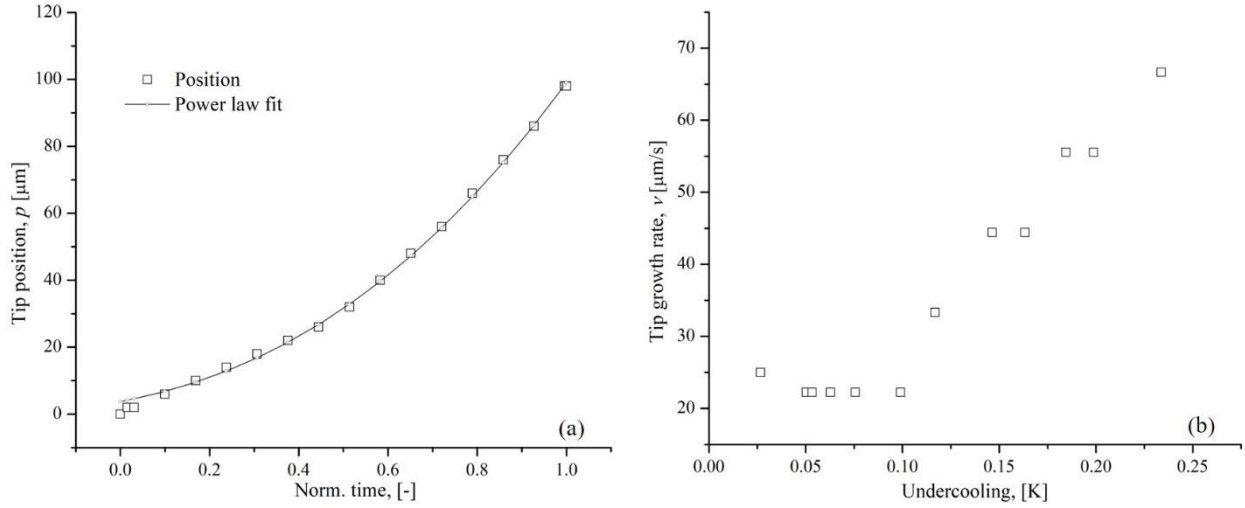

Figure 5: Estimated tip growth rate as a function of **(a)** time, and **(b)** undercooling for the $G1000\dot{T}1$ case. The fitted power law for the tip position in (a) is shown as a solid line: $p = 3.8(t^{2.5})$. The growth rate as a function of undercooling in (b) also shows a non-linear trend.

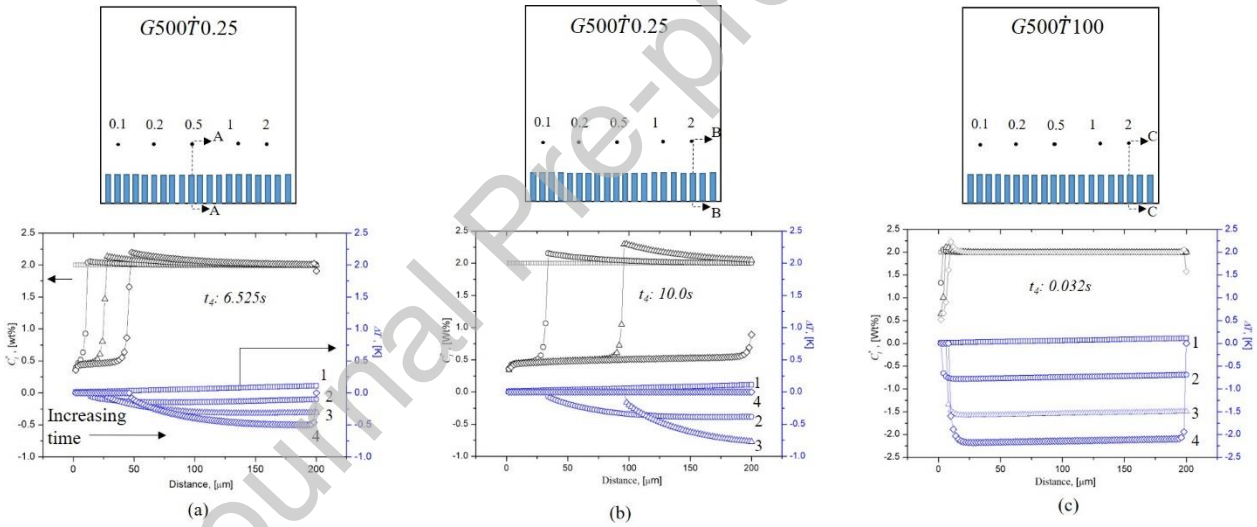

Figure 6: Solute and undercooling profile ahead of the growing columnar grains for *G*500 series as a function of distance. The profile extends from the bottom of the domain to the locus of the linear array of inoculants (at 200 μm for undercooling as marked). The profile is for different time-stamps, where time is normalized for a given simulation condition. **(a)** $G500\dot{T}0.25$ for the middle inoculant (section A-A), **(b)** $G500\dot{T}0.25$ for the right-hand most inoculant (section B-B), and **(c)** $G500\dot{T}100$ for the right-hand most inoculant (section C-C). The scales for plots have been kept the same for comparison. Numbers 1-4 indicate the different time-stamps at which the data is presented. 1 indicates the time very early in the columnar grain growth and 4 represents the time when the inoculant is activated. 2 and 3 represents times that are almost equally divided between 1 and 4. t_4 for each run is shown in the inset in each figure. Curve 4 in (b) represents columnar growth extending to the inoculant position with undercooling not sufficient to activate the inoculant.

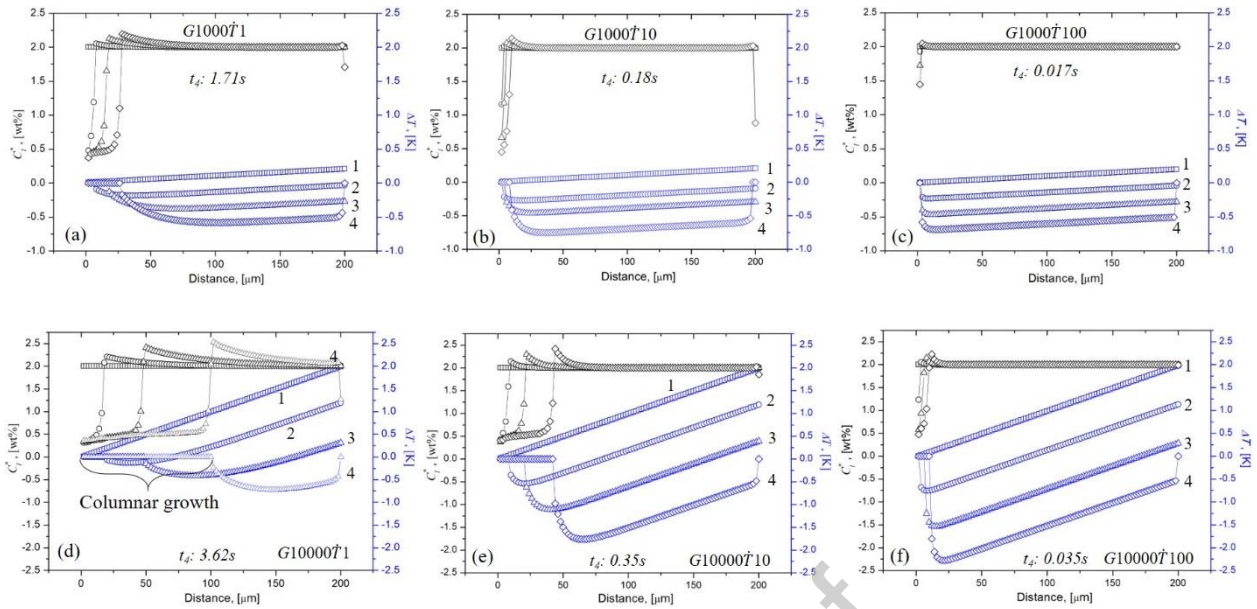

Figure 7: Similar plot as Figure 6 for *G*1000 and *G*10000 series. All plots are for the middle inoculant (as in Figure 6a). (**a-c**) *G*1000 for $\dot{T}$ = 1, 10 and 100 Ks^{-1}, respectively. (**d-f**) *G*10000 for $\dot{T}$ = 1, 10 and 100 Ks^{-1}, respectively. The scale has been kept the same for a given series for better comparison.

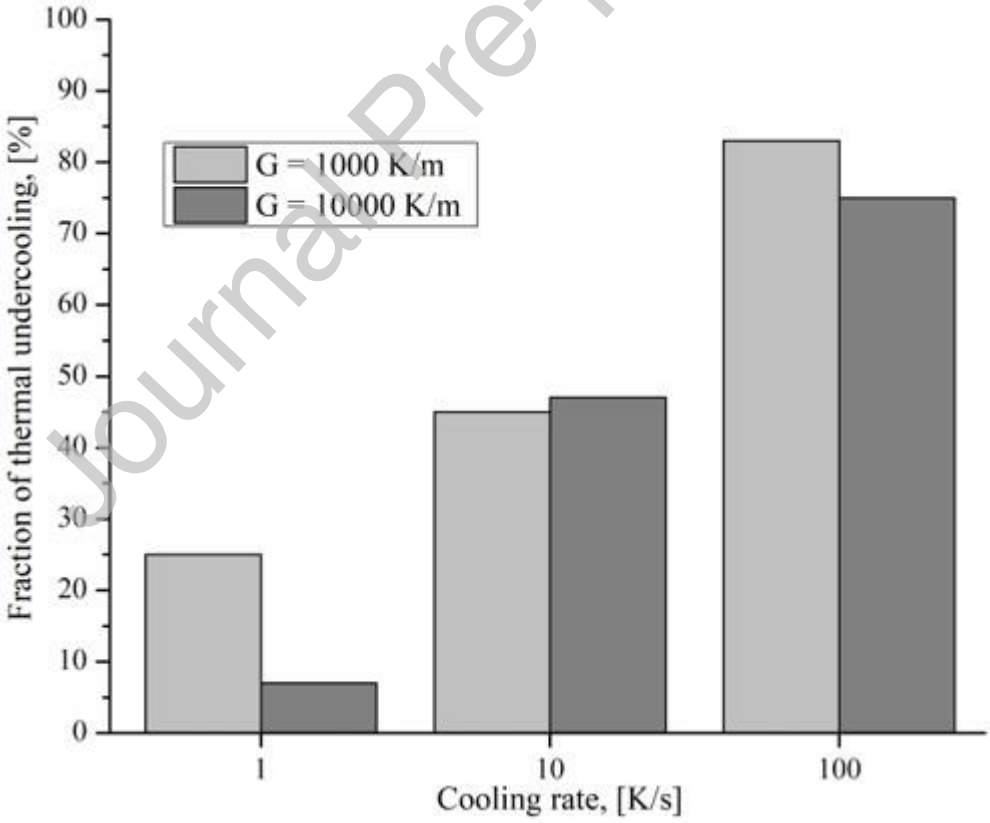

Figure 8: Calculated percentage contribution of thermal undercooling available for the Inoculant No. 3 of the total undercooling as a function of cooling rate at two thermal gradient conditions. The contribution of thermal undercooling to the total undercooling is more pronounced at a higher cooling rate and is suppressed at a higher thermal gradient.

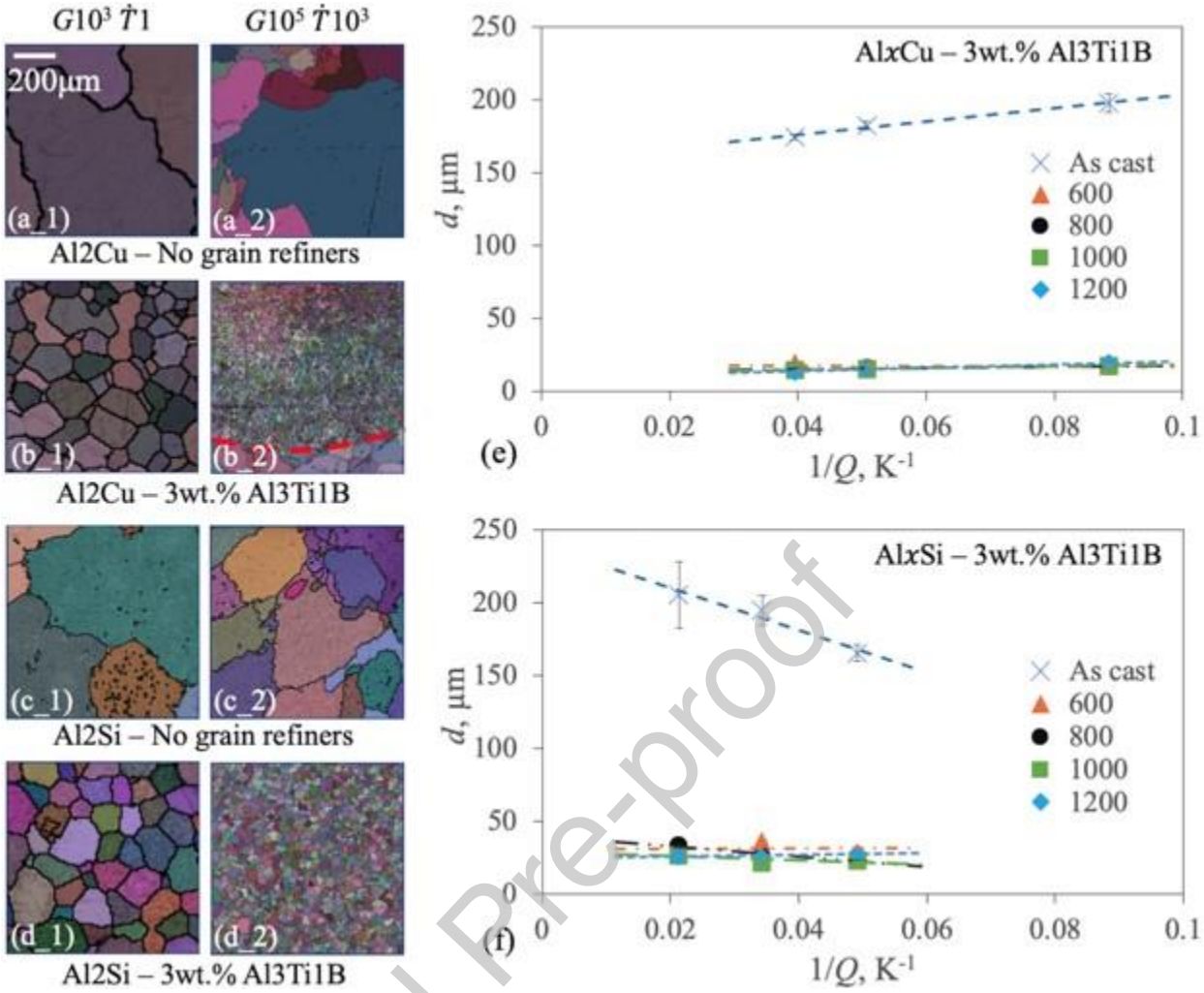

Figure 9: Grain morphology, using electron backscatter diffraction (EBSD), of **(a)** Al-2Cu system without grain refiner addition for (a_1) as cast and (a_2) laser surface re-melted (LSR) conditions, **(b)** Al-2Cu system with 3wt.% Al3Ti1B grain refiner addition for (b_1) as cast and (b_2) LSR conditions, **(c)** Al-2Si system without grain refiner addition for (c_1) as cast and (c_2) LSR conditions, and **(d)** Al-2Si system with 3wt.% Al3Ti1B grain refiner addition for (d_1) as cast and (d_2) LSR conditions. Grain size vs $1/Q$ for **(e)** AlxCu with 3wt.%Al3Ti1B, and **(f)** AlxSi with 3wt.%Al3Ti1B. Here, (e) and (f) shows results for as cast and LSR samples which were run with four scan speeds of 600, 800, 1000 and 1200 mm/min. Grain morphology results shown in (a-d) are of as cast and 600 mm/min scan speed samples with related G & $\dot{T}$ of 10^3 Km^{-1} & 1 Ks^{-1} and 10^5 Km^{-1} & 10^3 Ks^{-1}, respectively. Furthermore, (e) and (f) show that a much larger number of inoculants are activated for nucleation (intercept of the line of best fit) and higher potency to activate nucleation (shallower slope of the line of best fit) due to increased growth rate, v, in LSR. Note: the red line in (b_2) marks the meltpool boundary.

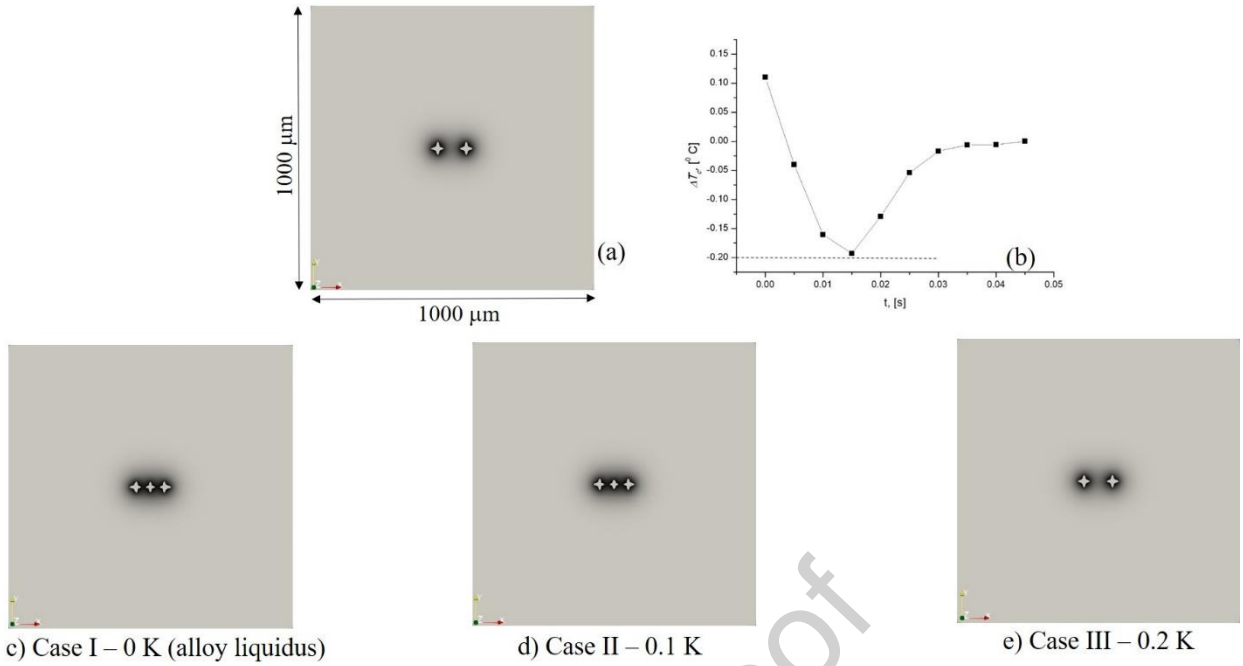

Figure A.1: Verification of the *µMatIC* modification - 2-grain approach: **(a)** Two grains placed in the computational domain are allowed to grow which results in **(b)** a maximum undercooling of <0.2 K at the mid-point. **(c-e)** The undercooling at the mid-point is tracked as a function of time. The maximum undercooling achieved is <~0.2 K.

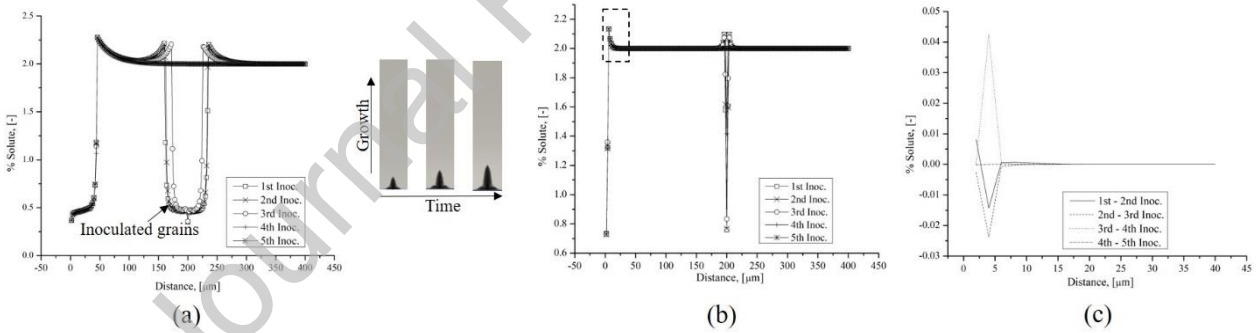

Figure B.1: Solute profile (presented horizontally with respect to the computational domain which is shown as a Growth-Time figure in the center) as a function of time ahead of the growing columnar grains for **(a)** $G1000\dot{T}1$ (t = 20000 s), and **(b)** $G1000\dot{T}100$ (t = 240 s). Only the columnar grains that had a nucleant placed ahead of them (@200 µm) were chosen. The five solute profiles are named according to the inoculant number starting from the left (Figure 1). **(c)** shows the difference in the solute content for the dotted box in (b).